Janus carbon shells with inner–outer functional asymmetry enable local proton enrichment for promoting CO_2 methanation

Liu Tengyi[1,†,*], Hou Xiaofan[1,†], Wijak Yospanya[1,†], Ye Songbo[1], Yasutaka Matsuo[2], Shimpei Ono[3], Reiko Oda[1,4], Li Hao[1,*], Hiroshi Yabu[1,*]

(1. *Advanced Institute for Materials Research (WPI-AIMR)*, *Tohoku University*, *2-1-1 Katahira*, *Aoba-Ku*, *Sendai*, 980-8577, *Japan*;
2. *Research Institute for Electronic Science (RIES)*, *Hokkaido University*, *N21W10*, *Kita-Ward*, *Sapporo*, 001-0021, *Japan*;
3. *International Center for Synchrotron Radiation Innovation Smart*, *Tohoku University*, *Sendai*, 980-8579, *Japan*;
4. *Univ. Bordeaux*, *CNRS*, *Bordeaux INP*, *CBMN*, *UMR* 5248, *IECB*, *F* 33600 *Pessac (France)*)

Abstract: Exploring non-copper electrocatalysts for CO_2-to-CH_4 electrosynthesis is important for reducing overreliance on copper and broadening the catalyst landscape. We report a strategy that enables CH_4 formation on cobalt phthalocyanine (CoPc) by regulating the local reaction microenvironment through the catalyst structure. Ultrathin hollow carbon nanospheres (HCNs) with a uniform size were synthesized and used as supports for CoPc, forming “Janus carbon shells” with inner–outer functional asymmetry. The resulting CoPc-HCN hybrid had a maximum CO_2-to-CH_4 selectivity of 15.1%, overcoming the conventional CO-selective behavior of CoPc. Mechanistic studies show that the hollow carbon structure induces a proton enrichment outside the shell through an inner–outer surface interaction. The inner carbon surface promotes the hydrogen evolution reaction (HER) and produces a proton-enriched environment near the CoPc-active outer surface, thereby enabling CO_2 methanation. This work highlights the critical role of catalyst structure in overcoming intrinsic selectivity limits of molecular catalysts.

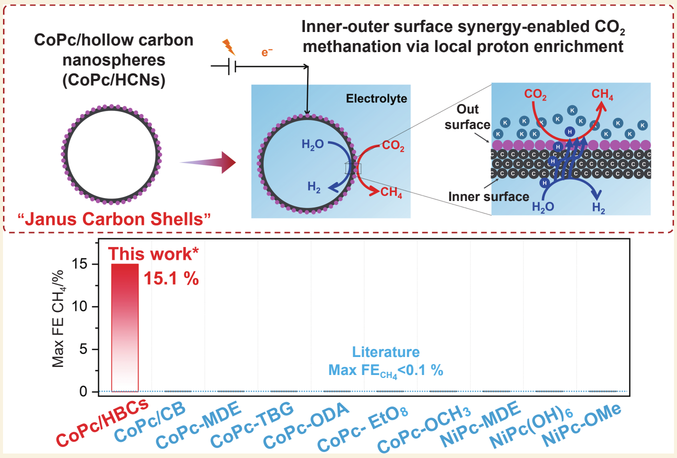

Key words: Electrochemical CO_2 reduction；Methane；Cobalt phthalocyanine；Janus carbon shells；Proton enrichment

1 Introduction

The continued reliance on fossil fuels has led to a rapid increase in atmospheric carbon dioxide (CO_2) concentration, posing severe risks to the environment and climate[1–3]. Electrochemical CO_2 reduction (ECR), when powered by renewable electricity, provides a promising pathway to convert CO_2 into value-added fuels and chemicals under mild conditions, thereby contributing to carbon neutrality and sustainable energy storage[4–10].

Among the products of ECR, deeply reduced carbon products are particularly attractive due to their high energy density and practical relevance[11–15]. Copper-based catalysts are currently the main systems capable of efficiently producing multi-carbon (C_{2+}) products, owing to their unique ability to promote C—C coupling[16–18]. However, the development of non-copper catalysts for deep CO_2 reduction remains highly desirable, especially for single-carbon (C_1) products such as methane (CH_4), which represent important synthetic fuels[12,13,19–22].

Molecular catalysts based on metal phthalocyanines (M-Pcs) and porphyrins, featuring well-defined

Received: February 05, 2026
Revised: April 05, 2026
Accepted: April 05, 2026

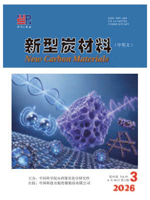

metal-nitrogen (M-N_4) active sites, have emerged as highly selective catalysts for CO_2-to-CO conversion[23–25]. In particular, cobalt phthalocyanine (CoPc) is widely reported as an efficient and robust CO-selective catalyst[23–24]. However, CH_4 formation on CoPc is generally considered unfavorable. The strong tendency for CO desorption, together with the lack of a proton-rich reaction environment hinders further hydrogenation steps beyond CO[11–13,26–27]. As a result, CH_4 production has been almost exclusively achieved on copper-based catalysts or specially designed copper phthalocyanines[28–30], leaving a critical gap in non-copper systems for CH_4 electrosynthesis.

Herein, we demonstrate a strategy to overcome this limitation by regulating the local reaction environment of CoPc through catalyst architecture. Specifically, we design Janus carbon shells with inner–outer functional asymmetry, in which the inner and outer carbon surfaces perform distinct yet coupled electrochemical functions. Hollow carbon nanospheres (HCNs) with uniform size and ultrathin carbon shells are synthesized and employed as supports for CoPc to realize this Janus architecture. The resulting CoPc/HCNs hybrid exhibits a maximum CO_2-to-CH_4 selectivity of 15.1%, breaking the conventional CO-selective behavior of CoPc. Mechanistic investigations reveal that the hollow carbon architecture induces local proton enrichment via an inner–outer surface synergy, where the inner carbon surface promotes hydrogen evolution and supplies protons to the CoPc-active outer surface. This locally proton-rich microenvironment enables CoPc to mediate CO_2 methanation providing a general strategy for promoting multi-electron CO_2 reduction on molecular catalysts.

2 Experiment section

2.1 Materials and characterization

In this work, CoPc (>99.9%) was supplied by Azul Energy Corporation. Ethanol, 2-propanol (IPA), dimethyl sulfoxide (DMSO), resorcinol, formaldehyde solution (36%–38%, mass fraction, the same below), and potassium hydroxide (>99.0%) were purchased from Fuji-Wako. Nafion dispersion solution (20%) and ammonia solution (25%) were obtained from Sigma-Aldrich, while tetraethyl orthosilicate was purchased from Tokyo Chemical Industry. Carbon paper gas diffusion layers for electrochemical CO_2 reduction were obtained from Mitsubishi Chemical Corporation (PYROFIL-GDL MFK-A, 0.21 mm). CO_2, CO, CH_4, C_2H_4 and H_2 gases were purchased from Taiyo Nippon Sanso, each with a purity above 99.9%. Ultrapure water with a resistivity of 1.82×10^7 Ω cm was produced using an ELGA Pure-lab system. All reagents were used as received without further purification.

Materials were processed using a planetary ball mill and ultrasonic dispersion, and catalyst inks were deposited onto substrates by ultrasonic spray coating. Electrochemical CO_2 reduction measurements were conducted using a Versa-STAT 4 electrochemical workstation, with gaseous products analyzed by GC-FID. Sample masses, drying, and gas flow rates were controlled using an analytical balance, oven, and gas flow meters, respectively. The prepared catalysts were characterized by XPS, XRD, and XAFS to investigate surface composition, crystalline structure, and local electronic structure. XAFS data were analyzed using ATHENA, and Fourier transformations of k^3-weighted EXAFS spectra were performed over a k-space range of 3–10 Å^{-1}, with the R-space range of 0–6 Å, or up to 10 Å when necessary, used for analysis.

2.2 Synthesis of hollow carbon nanospheres (HCNs)

As shown in Fig. 1, the synthesis was modified from a previously reported procedure[31]. In general, to a 300 mL round-bottom flask, ethanol/water mixture (volume ratio = 2 : 1, 100 mL) and ammonia (25%, 3.40 mL, 50.0 mmol) were mixed and stirred at 30 °C until the temperature was stable (~ 30 min). Then, tetraethyl orthosilicate (TEOS, 3.55 mL, 16.0 mmol) was added. Ten minutes later, resorcinol (495 mg, 4.50 mmol) was added, and another 10 min later, formaldehyde (36%–38%, 0.662 mL, about 9.0 mmol) was added. The dispersion was stirred at 30 °C for about 1 day (light brown dispersion), and the temper-

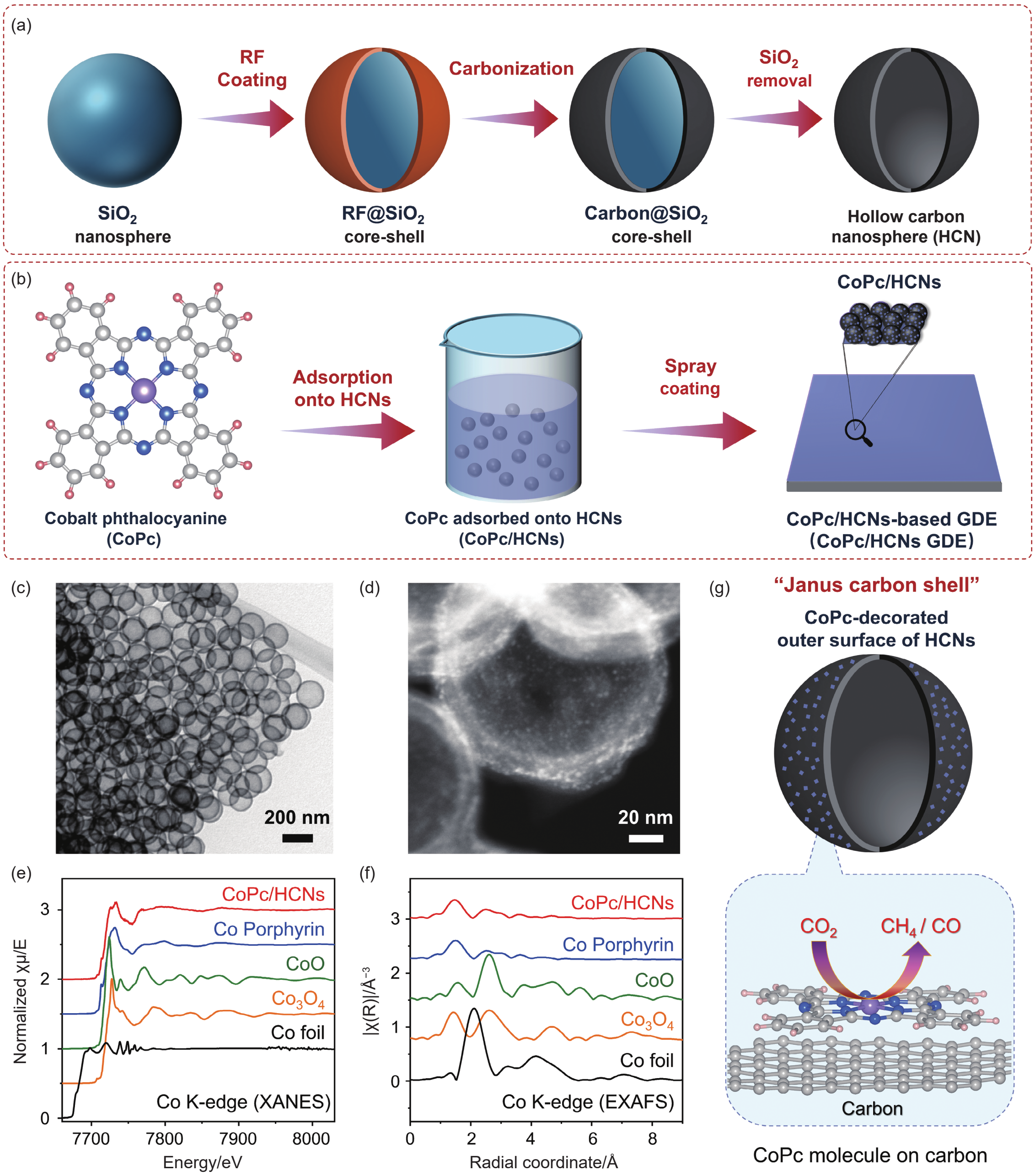

Fig. 1 Schematic illustration of the synthesis of hollow carbon nanospheres (HCNs) and the fabrication of CoPc-based electrocatalysts for electrochemical CO_2 reduction (ECR). (a) Schematic illustration of HCNs synthesis. (b) Schematic illustration of CoPc immobilization on HCNs. TEM images of (c) HCNs and (d) CoPc/HCNs. (e) Co K-edge XANES spectra of CoPc/HCNs and reference samples. (f) Corresponding Co K-edge EXAFS spectra. (g) Proposed structural model of the CoPc/HCNs hybrid, illustrating the Janus carbon shell architecture

ature was raised to 100 °C for another 1 day (dark brown dispersion). After cooling down, the dispersion was centrifuged (10 000 × g, 20 min, 20 °C), and the supernatant was washed twice with water and twice with ethanol to ensure the removal of resorcinol-formaldehyde (RF) polymer that was not associated with the nanoparticles. The sample was dried at 120 °C to yield dark brown powder of silica/RF polymer core-shell nanoparticles (SiO_2@RF NPs).

Next, carbonization of SiO_2@RF NPs was performed at 750 °C under vacuum for 60 min to afford silica/carbon core-shell nanoparticles as a black powder (SiO_2@C NPs, 1.148 mg). Finally, the silica was removed from SiO_2@C NPs under basic conditions to yield hollow carbon nanospheres (HCNs). SiO_2@C NPs was dispersed in KOH (6 mol L^{-1}, 23 mL, about 50 mg/mL). The dispersion was stirred at 60 °C for 1 day. The dispersion was centrifuged (10,000 × g, 20 min, room temperature), and the supernatant was replaced by water for 3 times to ensure the removal of KOH. After the final removal of supernatant, the sample was lyophilized to yield black powder (HCNs, 391.4 mg). The yield was estimated based on the number of carbon atoms of resorcinol (6) and formaldehyde (1) and the assumption that final HCNs consists of pure graphitic carbon. As a result, the yield of the whole process was estimated to be 90.1%.

2.3 Preparation of CoPc/HCNs electrodes

In this work, CoPc/HCNs catalysts were prepared using a method further refined from our previous report[32]. For instance, a 20% (mass fraction) CoPc/HCNs catalyst was synthesized by first dissolving 200 mg of CoPc in 150 mL of DMSO in a round-bottom flask, followed by the addition of 800 mg of HCNs, maintaining a total solid mass of 1000 mg. This fixed solid-to-solvent ratio was kept constant across all samples. The resulting mixture was sonicated in an ice-water bath for 30 min to promote the adsorption of CoPc onto the HCNs surface. Sonication was carried out using a probe sonicator set to an amplitude of 1 and a 30% pulse cycle, as higher amplitudes may promote dissolution of CoPc rather than its adsorption onto HCNs.

After adsorption, the mixture was filtered, and the solid cake was washed 3 times with methanol, then dried at a moderate temperature (e.g., 35 °C) in a vacuum oven for 24 h to preserve catalytic activity. The dried product was ground using a mortar, weighed, and transferred to a ball-mill autoclave. The ball-milling solvent consisted of DMSO (9 mL), IPA (9 mL), H_2O (4.5 mL) and Nafion (20%, 0.1 mL per 50 mg catalyst). Ball milling was conducted at 400 r/min for 5 min, followed by reverse rotation for another 5 min, repeated for a total of 30 min to reduce carbon agglomeration. After milling, the ball-mill autoclave was rinsed with a solvent mixture containing DMSO (9 mL), IPA (45 mL), and H_2O (13.5 mL), bringing the total solvent volume to 90 mL. The resulting mixture was then ultrasonically dispersed for at least 30 min to obtain a uniform catalyst ink.

The resulting ink was spray-coated onto carbon paper to fabricate the CoPc/HCNs hybrid electrode. Different catalyst loadings were achieved by adjusting the ink concentration and the number of spray passes. A slim-coating system (Flex-Coat Max, Sono-Tek) was used for spray-coating. Specifically, 25 mL of ink was loaded into a tempered glass container, and computer-controlled feeding delivered the ink to an ultrasonic nozzle (original Sono-Tek component), with dry, oil-free air at 551.6 kPa (80 PSI) propelling the ink droplets onto the carbon substrate. The substrate was masked using a stainless-steel square stencil (6 cm × 6 cm) to define the catalyst deposition area and was heated on a hot plate at 70 °C to facilitate solvent evaporation and promote uniform spray-deposition/growth of the catalyst across the carbon substrate surface. Catalyst loading was tuned by either increasing the ink concentration or the number of spray coatings. However, an ink concentration of >1 000 mg/90 mL might lead to nozzle clogging. Therefore, a standard ink formulation of 300 mg CoPc/HCNs dispersed in 90 mL of solution—corresponding to 60 mg of CoPc—was adopted to ensure stable and consistent spray performance. In this study, 1–4 spray passes were identified as the optimal condition for uniform electrode fabrication, the loading of CoPc/HCNs was approximately 0.02 mg cm^{-2} per spray pass.

2.4 Electrochemical CO_2 reduction and product analysis

Electrochemical CO_2 reduction tests were conducted using a custom three-electrode flow electrolyzer, similar to our previously reported setup[32]. The prepared MFK-A gas diffusion electrode was used as the cathode with an exposed area of 0.5 cm^2, Hg/HgO (1.0 mol/L KOH) as the reference electrode, and Pt wire as the counter electrode. The cathode and anode chambers were separated by a Nafion-117 membrane and filled with 1.0 mol/L KOH electrolyte. CO_2 was supplied from the back side of the GDE at a controlled flow rate, typically 15 mL/min, to maintain a stable gas-liquid-solid interface. Standard ECR measurements were performed for approximately 900 s using 25 mL electrolyte in each chamber, while long-term durability tests were carried out with electrolyte circulation.

The gas products were collected in gas bags and analyzed by gas chromatography. H_2, CH_4, and CO were detected by TCD, while C_2H_4 was detected by FID. Product concentrations were quantified using calibration curves obtained from standard gas mixtures, all showing R^2 values above 0.99. Faradaic efficiencies and partial current densities were calculated from the measured gas amounts, total charge, and electrode area. The applied potentials were converted to the RHE scale according to:

$$E(\text{vs.RHE}) = E(\text{vs.Ref.}) + 0.0592 \times \text{pH} + E_0(\text{Ref.}) - iR$$

2.5 Computational methods

DFT calculations were performed using the Vienna Ab initio Simulation Package (VASP) to investigate the electronic and magnetic properties of the systems. The RPBE functional within the generalized gradient approximation was used, with a plane-wave cutoff energy of 520 eV. Spin-polarized calculations were conducted, and the electronic and ionic convergence criteria were set to 1×10^{-6} eV and 0.05 eV $Å^{-1}$, respectively. Van der Waals interactions were included using the DFT-D3 method with Becke–Johnson damping. Adsorbate binding and free energies were calculated using the most stable adsorbate configurations. Solvation corrections of −0.25 eV for *COOH and −0.10 eV for *CO were applied, and zero-point energy, entropy, and heat capacity corrections were included following previous reports. Activity volcano plots were constructed based on our previous work[32].

3 Results and discussion

3.1 Structure analysis

In this work, hollow carbon nanospheres (HCNs) were synthesized following a previously reported procedure with slight modifications[31]. Briefly, monodisperse SiO_2 nanospheres were first prepared by a facile chemical route (Fig. 1a). Subsequently, a resorcinol–formaldehyde (RF) polymer layer was coated onto the SiO_2 nanospheres, yielding RF@SiO_2 core–shell structures. High-temperature pyrolysis of RF@SiO_2 was then conducted under vacuum to carbonize the RF shell, forming carbon@SiO_2 core–shell nanoparticles. Finally, the SiO_2 cores were selectively removed under alkaline conditions, resulting in hollow carbon supports. Detailed synthesis procedures are provided in the Experiment section.

The obtained HCNs were used as a support for cobalt phthalocyanine (CoPc) following our previously reported protocol (Fig. 1b)[25,32]. CoPc powder was dispersed in a DMSO solution containing HCNs, allowing molecular adsorption of CoPc onto the carbon surface. After filtration and thorough rinsing with methanol, the hybrid was vacuum-dried at 35 °C overnight, ground into a fine powder, and stored under vacuum. For fabricating the gas diffusion electrode (GDE) , the catalyst was ball-milled to ensure homogeneous dispersion, formulated into an ink, and spray-coated onto hydrophobic carbon paper to yield CoPc/HCNs-based GDEs.

High-resolution transmission electron microscopy (HR-TEM) was used to examine the morphology of the hollow carbon support (Fig. 1c and Fig. S1). The HCN particles exhibit a uniform spherical morphology with an average diameter of approximately 170 nm (Fig. S2), indicating good size uniformity and suggesting the scalability of the synthetic method. Moreover, no obvious structural damage was observed after alkaline removal of the SiO_2 core, indicating that the hollow carbon shell remains intact and accessible to electrolyte transport, consistent with previous reports of loosely packed, non-sealed carbon shells containing transport channels[31]. The molecular structure of the CoPc used in this study was further confirmed by XRD, XPS and UV–Vis–NIR spectroscopy (Fig. S3–S6). The XRD pattern matches well with that of standard β-phase cobalt phthalocyanine (β-CoPc) (Fig. S3), in agreement with our previous report[24]. The XPS results further verify the characteristic bonding configuration of CoPc: the C 1s spectrum can be deconvoluted into C—C/C=C and C—C=N components, while the N 1s spectrum consists of pyrrolic-N and bridge-N species (Fig. S4 and S5). The corresponding peak-area ratios agree well with the theoretical values expected from the CoPc molecular structure, supporting the successful synthesis of structurally intact CoPc. In addition, the UV–Vis–NIR spectrum displays the characteristic absorption features of phthalocyanine species (Fig. S6). These results collectively confirm that the synthesized CoPc corresponds to the standard β-phase CoPc with the expected molecular and spectroscopic characteristics. After CoPc loading, the hollow carbon structure remained intact (Fig. 1d), while bright contrast spots corresponding to molecular-level dispersion of CoPc sites were observed on the carbon surface, consistent with our previous reports[25,32].

To probe the local electronic structure of the Co centers, X-ray absorption fine structure (XAFS) measurements were performed. As shown in Fig. 1e, the X-ray absorption near-edge structure (XANES) spectra indicate that both CoPc and Co porphyrin (CoPr) exhibit absorption edge positions and near-edge features that are more similar to those of CoO than to metallic Co foil or Co_3O_4. Specifically, Co foil shows the characteristic edge feature of metallic Co at lower energy, whereas Co_3O_4 displays a sharper absorption feature. These results suggest that the average oxidation state of Co in both CoPc and CoPr is close to +2. Extended X-ray absorption fine structure (EXAFS) analysis was further carried out to investigate the local coordination environment of the Co centers (Fig. 1f). In the Fourier-transformed EXAFS spectra, Co foil exhibited a pronounced Co–Co coordination peak at $R \approx 2.1$ Å, whereas Co_3O_4 and CoO showed Co–O coordination peaks at $R \approx 1.7$ Å. In contrast, both CoPc and CoPr displayed a distinct first-shell peak at a different radial distance, indicating that the Co centers were coordinated by light elements rather than Co neighbors. Noticeable differences remain in the higher-shell region from 2 to 4 Å, where CoPc showed more pronounced oscillations. These differences may arise from enhanced multiple-scattering effects, local structural distortion, and variations in the Co–N bond-length distribution associated with differences in the macrocyclic backbone. Collectively, these results demonstrate that CoPc molecules are successfully immobilized on the hollow carbon support while maintaining their molecular structure and coordination environment.

Based on these observations, a structural model is proposed in which CoPc molecules are molecularly dispersed on the outer surface of the hollow carbon (Fig. 1g). This configuration provides the structural basis for inner–outer functional asymmetry, a defining characteristic of the “Janus carbon shell”. These results suggest that the molecularly dispersed CoPc sites are likely responsible for the subsequent ECR activity observed for the CoPc/HCNs system.

3.2 Electrocatalytic CO_2 reduction performance

The ECR performance of the catalysts was evaluated using a gas-fed electrolyzer identical to that employed in our previous work (Fig. 2a and Scheme S1)[23,25,33], with the fabricated GDEs serving as cathodes. We first compared CoPc supported on hollow carbon (CoPc/HCNs) with CoPc supported on solid carbon@SiO_2 (CoPc/C@SiO_2) nanospheres (Fig. 2b).

For CoPc/C@SiO_2, the catalytic behavior closely resembled that of previously reported CoPc/Ketjen black (CoPc/KB) systems[23–24]. CO is the dominant product, and its Faradaic efficiency (FE) increases with increasing spray passes (Fig. 2c) or catalyst loading (Fig. S7). This trend can be attributed to the progressive dominance of CoPc active sites over carbon sites that favor the hydrogen evolution reaction (HER) at low loadings. Moreover, multilayer stacking of CoPc molecules further promotes CO formation.

To our surprise, CoPc/HCNs exhibited a markedly different product distribution compared with solid carbon–supported counterparts. In addition to CO, CH_4 was detected as a significant product, particularly at low catalyst loadings (Fig. 2d and Fig. S8-9). Given that CH_4 formation is an eight-electron deep-reduction process and is generally considered unfavorable on CoPc, this observation is highly intriguing. Notably, the CO_2-to-CH_4 conversion proceeds through a complex multi-step proton-coupled hydrogenation

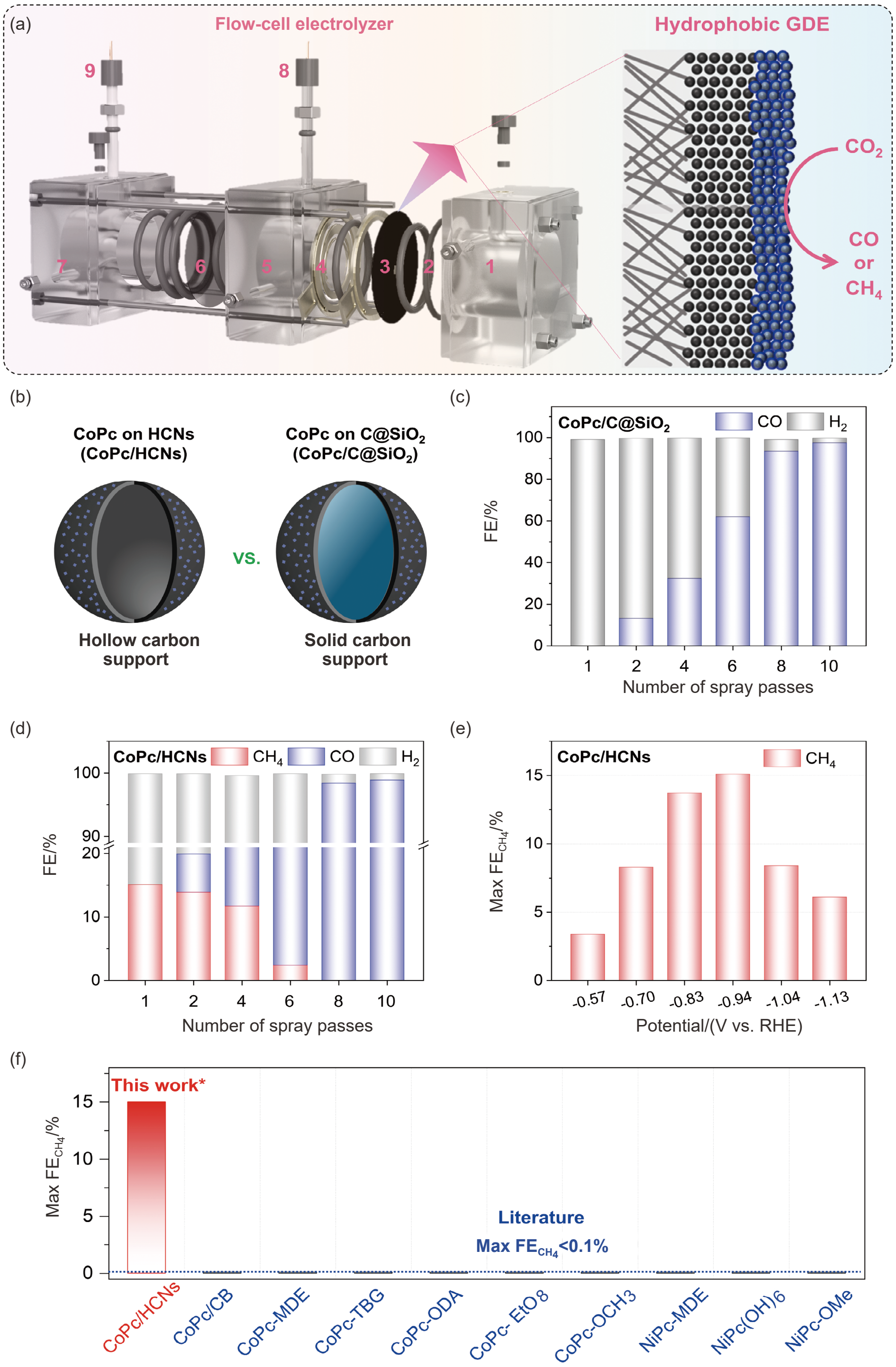

Fig. 2 ECR performance of CoPc/HCNs electrodes. (a) Schematic illustration of the flow-cell electrolyzer and gas diffusion electrode. (b) Structural models of CoPc/HCNs and CoPc/C@SiO$_2$ hybrids. ECR performance of (c) CoPc/C@SiO$_2$ hybrid and (d) CoPc/HCNs hybrid at spray passes (catalyst loadings). (e) Potential-dependent ECR performance of the CoPc/HCNs hybrid. (f) Maximum Faradaic efficiency (FE) of CH_4 achieved on our CoPc/HCNs hybrid compared with previously reported Pc-based catalysts from the literature

pathway (Fig. S10 and S11), highlighting the stringent microenvironmental requirements for CH_4 generation. In detail, at low CoPc loadings—especially with a single spray pass—CoPc/HCNs display pronounced CH_4 selectivity. In sharp contrast, solid carbon–supported catalysts, including CoPc/C@SiO$_2$ and CoPc/KB, exclusively produce H_2 under identical conditions, indicating that the hollow carbon architecture plays a decisive role in enabling CH_4 formation beyond the intrinsic nature of CoPc. As the CoPc loading increases, CO gradually becomes the dominant product, consistent with the well-established tendency of multilayer CoPc to favor CO formation.

Potential-dependent measurements of the single-pass CoPc/HCNs electrode reveal a volcano-shaped CH_4 selectivity trend (Fig. 2e), reaching a maximum CH_4 Faradaic efficiency of 15.1% at −0.94 V (vs. RHE). At lower overpotentials, sluggish reaction kinetics limit CH_4 formation, whereas at more negative potentials, HER becomes increasingly competitive. Notably, comparison with previously reported CoPc-based catalysts from the literature shows negligible CH_4 production (Fig. 2f, Table 1 and Table S2), highlighting the unique behavior of our CoPc/HCNs system.

In addition, under N_2 atmosphere, the CoPc/HCNs catalyst only produced H_2, and no CH_4 or other carbon-containing products were detected, indicating that the carbon in the observed CH_4 was derived from CO_2 gas (Fig. S12). Moreover, the CoPc/HCNs catalyst exhibited good stability under operating conditions. At a current density of −150 mA cm^{-2}, the catalytic system remained stable for approximately 23 h (Fig. S13), with essentially unchanged catalytic performance throughout the test, further confirming the good stability of the CoPc/HCNs catalyst. Post-reaction XPS characterization further revealed that the characteristic signals associated with CoPc remained clearly visible after electrolysis, indicating that the Co–N_4 active sites were well preserved and that no obvious leaching of CoPc occurred during the reaction (Fig. S14). These results exclude catalyst instability and extraneous carbon sources as the origin of CH_4 formation, and instead highlight the important role of the hollow carbon support in modulating the reaction environment.

Taken together, these results suggest that although CoPc intrinsically favors CO production, the hollow carbon support fundamentally alters the reaction microenvironment, enabling CH_4 formation. Given that CH_4 generation requires extensive proton-coupled electron transfer and C—H bond formation, we hypothesize that local proton enrichment induced by the hollow carbon architecture plays a critical role.

3.3 Role of hollow carbon in proton supply

To elucidate the contribution of the hollow carbon support, we first compared the electrochemical behavior of HCNs and solid C@SiO_2 in 1 mol L^{-1} KOH electrolyte under CO_2 atmosphere (Fig. 3a). Both materials exclusively catalyze HER in KOH solution (Fig. 3b), confirming their inertness toward CO_2 reduction.

Notably, HCNs exhibit a significantly higher current density than solid C@SiO_2 nanospheres, indicative of a larger electrochemical surface area (ECSA). The electrochemical double-layer capacitance (C_{dl})

Table 1 Comparison of the key parameters in this work and selected literature

Catalyst	pH	Max FE_{CH_4} %	Max FE_{CO} %	Ref.
CoPc/HCNs	14.0	15.1	>98.0	This work*
CoPc/CP	14.0	0	>98.0	Our work[24]
CoPc/KB	14.0	0	>98.0	Our work[23]
CoAzPc-4N/KB	14.0	0	>98.0	Our work[25]
CoPc/CNT-MDE	6.8	0	98.0	[39]
CoPc/CNT-MDE	2.0	0	73.0	[40]
CoPc/CB-MDE	7.8	0	98.0	[41]
CoPc/CNT-MDE	6.8	0	97.0	[42]
CoPc/CNT-ODA	7.3	0	97.7	[43]
CoPc-TBG/CNT	14.0	0	96.0	[44]
CoPc-EtO_8/CNP	7.8	0	95.0	[45]
CoPc-OCH_3/CNT	7.3	0	97.0	[46]
CoPPc/CNT	7.3	0	90.0	[47]
NiPc/CNT-MDE	7.3	0	>98.0	[48]
NiPc/NHCSs	7.3	0	>98.0	[49]
NiPc$(OH)_6$(DCNFO)/CNT	14.0	0	>98.0	[50]
NiPc-OMe	2.0	0	>98.0	[51]

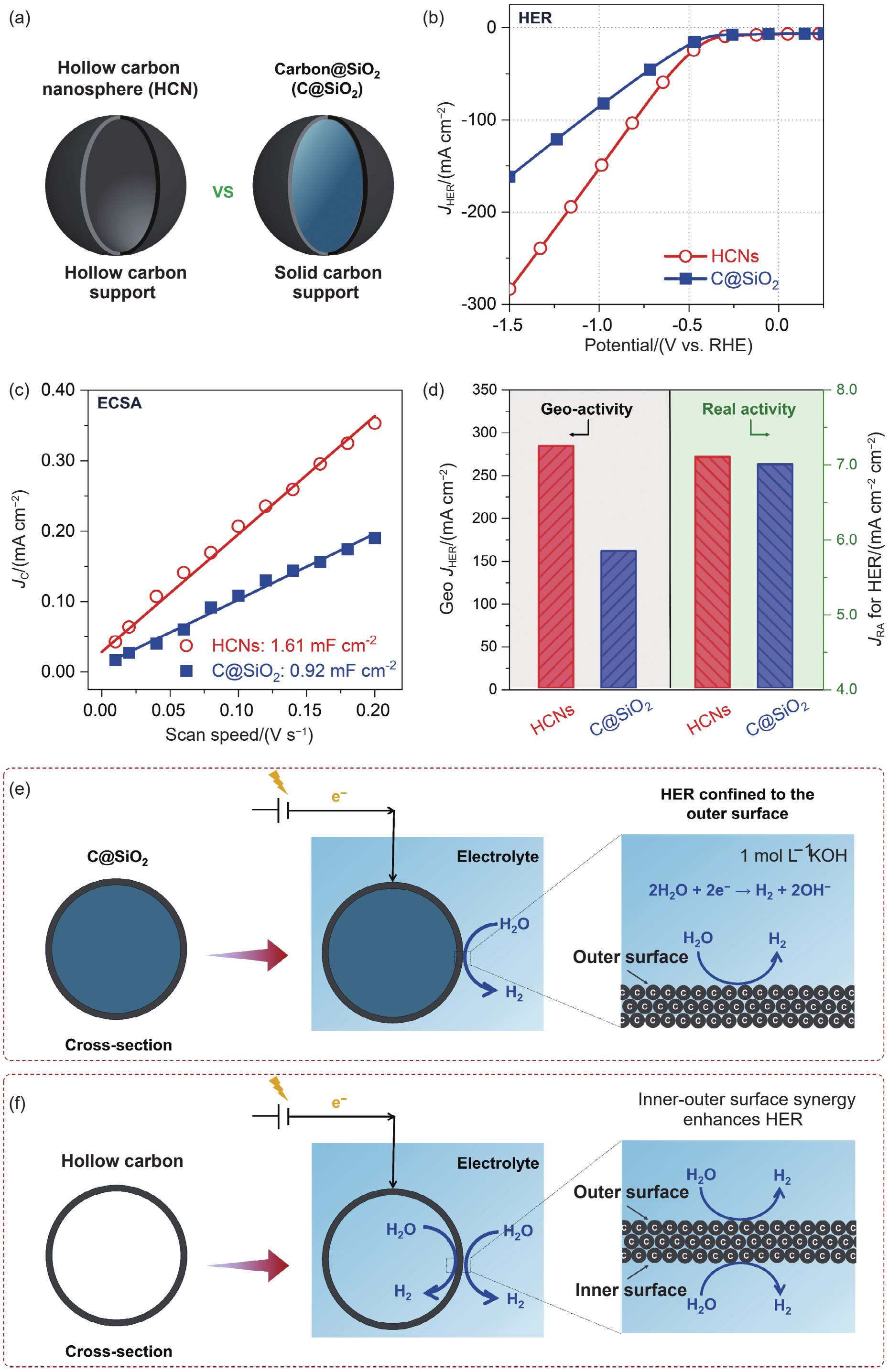

Fig. 3 Electrocatalytic performance of HCNs and C@SiO_2 electrodes. (a) Structural models of HCNs and C@SiO_2. (b) LSV curves of HCNs and C@SiO_2 electrodes under CO_2 atmosphere, showing exclusive hydrogen evolution reaction (HER) activity. (c) Electrochemical double-layer capacitance (C_{dl}) as a function of scan rate for HCNs and C@SiO_2 electrodes, used to estimate the electrochemical surface area (ECSA). (d) Comparison of geometric current density and ECSA-normalized current density (intrinsic activity) of HCNs and C@SiO_2 electrodes. (e-f) Schematic illustrations of electrocatalytic reactions occurring on the outer surface of solid C@SiO_2 (e) and the inner–outer surface synergy of hollow HCNs (f)

measurements further corroborate this observation[34–35]. The hollow carbon shows a C_{dl} value of 1.61 mF cm^{-2}, compared to 0.92 mF cm^{-2} for C@SiO_2, corresponding to ECSA values of 40.3 and 23.0 cm^2 cm^{-2}, respectively (Fig. 3c and Fig. S15-16).

Geometric current densities at identical potentials reveal that hollow carbon delivers a current density of 284 mA cm^{-2}, approximately 1.8 times higher than that of solid C@SiO_2 (161 mA cm^{-2}) (Fig. 3d). However, when normalized to ECSA, both materials exhibit similar intrinsic activities, indicating that the enhanced performance originates from increased accessible surface area rather than altered catalytic nature.

These results lead to the schematic illustration shown in Fig. 3e and 3f. In solid C@SiO_2, only the outer carbon surface is electrochemically active due to the insulating SiO_2 core. In contrast, removal of the SiO_2 core enables electrolyte penetration into the hollow structure, activating both the inner and outer carbon surfaces as electrochemically accessible reaction centers. This electrochemical accessibility of spatially separated surfaces confirms the hollow carbon support functions as a Janus carbon shell, in which the inner and outer surfaces are electrochemically coupled yet play distinct roles.

3.4 Mechanistic insights into CH_4 formation

Density functional theory (DFT) calculations were conducted to elucidate reaction selectivity. The adsorption free energies of H* on CoPc/C and pristine carbon (graphite) were calculated to be 0.16 and 1.30 eV, respectively (Fig. 4a), indicating weak hydrogen adsorption on both sites. For ECR intermediates, CoPc/C exhibits favorable adsorption energies of

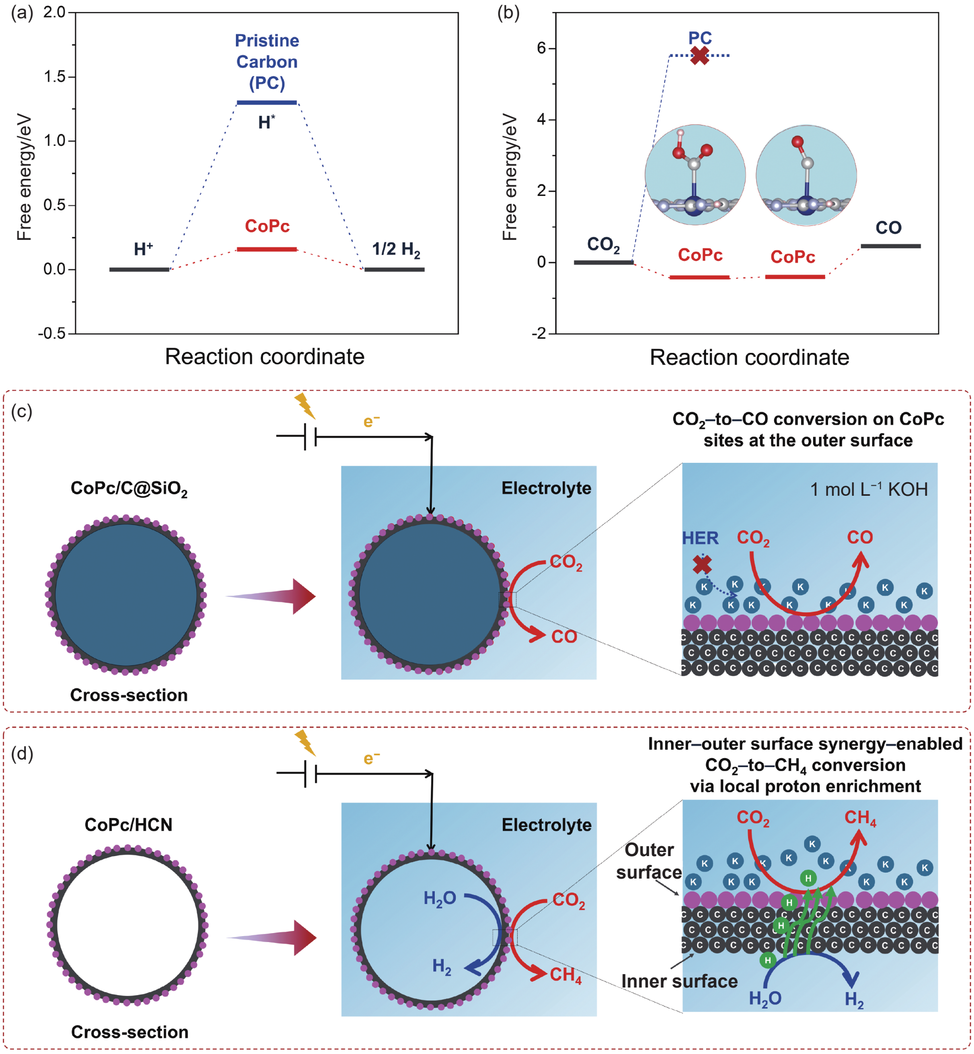

Fig. 4 Mechanistic insights into CH_4 formation on CoPc/HCNs hybrid. (a) DFT-calculated adsorption free energies of H* for CoPc/HCNs and pristine carbon. (b) DFT-calculated adsorption free energies of key CO_2 reduction intermediates (*COOH and *CO) on CoPc/HCNs and pristine carbon. (c) Schematic illustration of electrocatalytic CO_2-to-CO conversion on CoPc sites at the outer surface of CoPc/C@SiO_2 hybrid, where K^+ enrichment suppresses HER. (d) Schematic illustration of electrocatalytic CO_2-to-CH_4 conversion enabled by inner–outer surface synergy in the CoPc/HCNs hybrid, leading to local proton enrichment for CO_2 methanation

−0.42 eV for *COOH and −0.40 eV for *CO (Fig. 4b), confirming its intrinsic activity toward CO_2-to-CO conversion[36–38]. This also explains why CoPc favors HER only under conditions where ECR is kinetically hindered. In contrast, pristine carbon shows strongly unfavorable adsorption toward these intermediates, rendering it incapable of catalyzing the CO_2 reduction.

In CoPc/C@SiO_2 systems, CoPc sites dominate ECR, while K^+ accumulation near the cathode enhances the local electric field, suppresses HER, and favors CO production (Fig. 4c). In the CoPc/HCNs system, however, a dual-surface mechanism emerges (Fig. 4d). CoPc molecules reside on the outer surface, where K^+ enrichment suppresses proton reduction. Simultaneously, the inner carbon surface preferentially catalyzes HER, generating protons that migrate through the ultrathin carbon shell toward the CoPc-active outer surface. This spatial separation, arising from the inner–outer functional asymmetry of the Janus carbon shell, creates a locally proton-enriched microenvironment that enables CoPc to catalyze the CO_2 methanation.

4 Conclusion

We demonstrate that Janus carbon shells with inner–outer functional asymmetry provide an effective platform for enabling deep CO_2 reduction on molecular catalysts. Hollow carbon nanospheres (HCNs) with a uniform size and ultrathin carbon shells are synthesized and employed as supports for cobalt phthalocyanine (CoPc), and the resulting CoPc/HCNs hybrid achieves a maximum CO_2-to-CH_4 selectivity of 15.1%. While most previously reported CoPc-based catalysts predominantly produce CO, our results show that CH_4 formation—generally considered unfavorable on CoPc —can be realized through nanoscale structural regulation. Systematic analyses and theoretical calculations reveal that this behavior originates from local proton enrichment induced by the Janus carbon shell architecture. Specifically, the inner carbon surface preferentially catalyzes hydrogen evolution and contributes to proton enrichment near the CoPc-active outer surface, thereby facilitating CO_2 methanation. Overall, this work highlights the critical role of carbon support architecture in regulating interfacial proton availability and provides a general strategy for promoting multi-electron CO_2 reduction on molecular catalysts.

Conflict of Interest Statement

The authors declare no conflict of interest.

Acknowledgements

This work was supported by JSPS-KAKENHI (JP23H00301, JP24K17741, JP25K01737, JP26K17914, and JP26K17934), JSPS Core-to-Core Program (JPJSCCA20250005), JST-MIRAI (JPMJMI25I1), MEXT-ARIM (JPMXP1223HK0074, JPMXP1224HK0103), the CNRS and Université de Bordeaux: the International Research Project on Chiral Field–Matter Interaction (IRP-ChiFiMI), the IdEx Bordeaux (Research Program GPR LIGHT), the Iketani Science and Technology Foundation, the Hirose Foundation, the Steel Foundation for Environmental Protection Technology, and the TOKYO PRIZE Carbon Reduction. We are grateful to Mrs. Hirai and Mrs. Mori of Hokkaido University for their valuable support in HR-TEM. We gratefully acknowledge the Center for Computational Materials Science, Institute for Materials Research, Tohoku University for the use of MASAMUNE-IMR (202412-SCKXX-0211 and 202412-SCKXX-0209) and the Institute for Solid State Physics (ISSP) at the University of Tokyo for the use of their supercomputers.

References

[1] Luna P D, Hahn C, Higgins D, et al. What would it take for renewably powered electrosynthesis to displace petrochemical processes?[J]. Science, 2019, 364: 350.

[2] Wang Z, Xia B, Reducing carbon dioxide efficiently to reuse and recycle it[J]. Nature, 2024, 626: 86–91.

[3] Li F, Thevenon A, Rosas-Hernández A, et al. Molecular tuning of CO_2-to-ethylene conversion[J]. Nature, 2020, 577: 509-513.

[4] She Z W, Kibsgaard J, Dickens C F, et al. Combining theory and experiment in electrocatalysis: Insights into materials design[J]. Science, 2017, 355: 4998.

[5] Wu Y, Jiang Z, Lu X, et al. Domino electroreduction of CO_2 to methanol on a molecular catalyst[J]. Nature, 2019, 575: 639-642.

[6] Liu B, Zhan S, Du J, et al. Revealing the mechanism of sp-N doping in graphdiyne for developing site-defined metal-free catalysts[J]. Advanced Materials, 2023, 35: 2206450.

[7] Tan M, Hua Q, Zhang C, et al. Creating abundant gas–solid–liquid triple-phase interfaces in hierarchical porous structure for efficient electrochemical CO_2 reduction[J]. Advanced Functional Materials, 2025, Early View: 2510570.

[8] Jin S, Hao Z, Zhang K, et al. Advances and challenges for the electrochemical reduction of CO_2 to CO: From fundamentals to industrialization[J]. Angewandte Chemie International Edition, 2021, 60: 20627-20648.

[9] Wakerley D, Lamaison S, Wicks J, et al. Gas diffusion electrodes, reactor designs and key metrics of low-temperature CO_2 electrolysers[J]. Nature Energy, 2022, 7: 130-143.

[10] Liu T, Hou X, Zhang D, et al. Strategically advancing semiconducting phthalocyanines as high-performance electrocatalysts for electrochemical CO_2 reduction[J]. ACS Applied Electronic Materials, 2026, 8: 2187-2197.

[11] Xiong L, Zhan S, Ciano L D, et al. Elucidating the donor/acceptor regulatory mechanism for CO_2 electroreduction[J]. Advanced Materials, 2026, 38: e12478.

[12] Xiong L, Fu X, Fan W, et al. Unveiling the nanoconfinement effect in CO_2 electroreduction to CH_4 over mesoporous Cu-CeO_2 nanospheres[J]. ACS Central Science, 2025, 11: 1902-1910.

[13] Xiong L, Fu X, Recent advances and challenges in electrochemical CO_2 reduction to CH_4[J]. Chinese Journal of Catalysis, 2025, 73: 39–61.

[14] Wang H, Tzeng Y K, Ji Y, et al. Synergistic enhancement of electrocatalytic CO_2 reduction to C_2 oxygenates at nitrogen-doped nanodiamonds/Cu interface[J]. Nature Nanotechnology, 2020, 15: 131-137.

[15] Qiu X F, Zhu H L, Huang J R, et al. Highly selective CO_2 electroreduction to C_2H_4 using a metal-organic framework with dual active sites[J]. Journal of the American Chemical Society, 2021, 143: 7242-7246.

[16] Dinh C T, Burdyny T, Kibria M G, et al. CO_2 electroreduction to ethylene via hydroxide-mediated copper catalysis at an abrupt interface[J]. Science, 2018, 360: 783-787.

[17] Sun Q, Jia C, Lu H, et al. Ampere-level electroreduction of CO_2 and CO[J]. Chemical Society Reviews, 2025, 54: 6973-7016.

[18] Jouny M, Hutchings G S, Jiao F, Carbon monoxide electroreduction as an emerging platform for carbon utilization[J]. Nature Catalysis, 2019, 2: 1062–1070.

[19] Sorokin A B, Phthalocyanine metal complexes in catalysis[J]. Chemical Reviews, 2013, 113: 8152–8191.

[20] Zhang Y, Zhang X, Jiao L, et al. Conductive covalent organic frameworks of polymetallophthalocyanines as a tunable platform for electrocatalysis[J]. Journal of the American Chemical Society, 2023, 145: 24230-24239.

[21] Yabu H, Nakamura K, Matsuo Y, et al. Pyrolysis-free oxygen reduction reaction (ORR) electrocatalysts composed of unimolecular layer metal azaphthalocyanines adsorbed onto carbon materials[J]. ACS Applied Energy Materials, 2021, 4: 14380-14389.

[22] Zhang D, Hirai Y, Nakamura K, et al. Benchmarking pH-field coupled microkinetic modeling against oxygen reduction in large-scale Fe-azaphthalocyanine catalysts[J]. Chemical Science, 2024, 15: 5123-5132.

[23] Liu T, Zhang D, Chu Y, et al. Breaking the single-molecule paradigm: Multilayer cobalt phthalocyanine/carbon core-shell structure as the superior active unit for CO_2-to-CO electroreduction[J]. Applied Catalysis B: Environmental, 2026, 381: 125852.

[24] Liu T, Zhang D, Hirai Y, et al. Surface charge transfer enhanced cobalt-phthalocyanine crystals for efficient CO_2-to-CO electroreduction with large current density exceeding 1000 mA cm^{-2}[J]. Advanced Science, 2025, 12: 202501459.

[25] Liu T, Hou X, Zhang D, et al. Ampere-level electrosynthesis of CO via well-defined pyridinic-N incorporated cobalt phthalocyanine[J]. Small, 2025, 21: e07824.

[26] Liu T, Yabu H, Copper nanoclusters derived from copper phthalocyanine as real active sites for CO_2 electroreduction: Exploring size dependency on selectivity-A mini review[J]. EcoEnergy, 2024, 419–432.

[27] Guan A, Chen Z, Quan Y, et al. Boosting CO_2 electroreduction to CH_4 via tuning neighboring single-copper sites[J]. ACS Energy Letters, 2020, 5: 1044-1053.

[28] Weng Z, Wu Y, Wang M, et al. Active sites of copper-complex catalytic materials for electrochemical carbon dioxide reduction[J]. Nature Communications, 2018, 9: 415.

[29] Zhang J, My Pham T H, Gao Z, et al. Electrochemical CO_2 reduction over copper phthalocyanine derived catalysts with enhanced selectivity for multicarbon products[J]. ACS Catalysis, 2023, 13: 9326-9335.

[30] Xu Y, Li F, Xu A, et al. Low coordination number copper catalysts for electrochemical CO_2 methanation in a membrane electrode assembly[J]. Nature Communications, 2021, 12: 2932.

[31] Fuertes AB, Valle-Vigón P, Sevilla M, One-step synthesis of silica@resorcinol-formaldehyde spheres and their application for the fabrication of polymer and carbon capsules[J]. Chemical Communications, 2012, 48: 6124–6126.

[32] Abe H, Hirai Y, Ikeda S, et al. Fe azaphthalocyanine unimolecular layers (Fe AzULs) on carbon nanotubes for realizing highly active oxygen reduction reaction (ORR) catalytic electrodes[J]. NPG Asia Materials, 2019, 11: 57.

[33] Liu T, Hou X, Yabu H, Realizing ampere-level electrochemical CO_2 Reduction using gas diffusion electrodes[J]. ACS Electrochemistry, 2025, 1: 2317–2325.

[34] Liu T, Ohashi K, Nagita K, et al. A tin oxide-coated copper foam hybridized with a gas diffusion electrode for efficient CO_2 reduction to formate with a current density exceeding 1 A cm^{-2}[J]. Small, 2022, 18: 2205323.

[35] Liu T, Diao P, Nickel foam supported Cr-doped $NiCO_2O4$/FeOOH nanoneedle arrays as a high-performance bifunctional electrocatalyst for overall water splitting[J]. Nano Research, 2020, 13: 3299–3309.

[36] Ye S, Liu F, She F, et al. Hydrogen binding energy is insufficient for describing hydrogen evolution on single-atom catalysts[J]. Angewandte Chemie International Edition, 2025, 64: e202425402.

[37] Wang Y, Zhang D, Sun B, et al. Divergent activity shifts of tin-based catalysts for electrochemical CO_2 reduction: pH-dependent behavior of single-Atom versus polyatomic structures[J]. Angewandte Chemie International Edition, 2025, 64: e202418228.

[38] Zhang D, Jia X, Wang Y, et al. Digital materials ecosystem: from databases to AI agents for autonomous discovery[J]. Chemical Science, 2026, 17: 5763-6244.

[39] Zhang X, Wu Z, Zhang X, et al. Highly selective and active CO_2 reduction electrocatalysts based on cobalt phthalocyanine/carbon nanotube hybrid structures[J]. Nature Communications, 2017, 8: 14675.

[40] Feng S, Wang X, Cheng D, et al. Stabilizing *CO_2 intermediates at the acidic interface using molecularly dispersed cobalt phthalocyanine as catalysts for CO_2 reduction[J]. Angewandte Chemie International Edition, 2024, 63: e202317942.

[41] Wang M, Loiudice A, Okatenko V, et al. The spatial distribution of cobalt phthalocyanine and copper nanocubes controls the selectivity towards C2 products in tandem electrocatalytic CO_2 reduction[J]. Chemical Science, 2023, 14: 1097-1104.

[42] Wu X, Sun JW, Liu PF, et al. Molecularly dispersed cobalt phthalocyanine mediates selective and durable CO_2 reduction in a membrane flow cell[J]. Advanced Functional Materials, 2022, 32: 2107301.

[43] Xiong L, Fu X, Zhou Y, et al. Precise site-hydrophobicity modulation for boosting high-performance CO_2 electroreduction[J]. ACS Catalysis, 2023, 13: 6652-6660.

[44] Wang M, Torbensen K, Salvatore D, et al. CO_2 electrochemical catalytic reduction with a highly active cobalt phthalocyanine[J]. Nature Communications, 2019, 10: 3602.

[45] Ren S, Lees EW, Hunt C, et al. Catalyst aggregation matters for immobilized molecular CO_2RR electrocatalysts[J]. Journal of the American Chemical Society, 2023, 145: 4414-4420.

[46] Huang M, Chen B, Zhang H, et al. Tailored local electronic environment of Co-N4 sites in cobalt phthalocyanines for enhanced CO_2 reduction reaction[J]. Small Methods, 2024, 4: 2301652.

[47] Han N, Wang Y, Ma L, et al. Supported cobalt polyphthalocyanine for high-performance electrocatalytic CO_2 reduction[J]. Chem, 2017, 3: 652-664.

[48] Zhang X, Wang Y, Gu M, et al. Molecular engineering of dispersed nickel phthalocyanines on carbon nanotubes for selective CO_2 reduction[J]. Nature Energy, 2020, 5: 684-692.

[49] Gong S, Wang W, Lu R, et al. Mediating heterogenized nickel phthalocyanine into isolated Ni-N3 moiety for improving activity and stability of electrocatalytic CO_2 reduction[J]. Applied Catalysis B: Environmental, 2022, 318: 121813.

[50] Jin Y, Zhan X, Zheng Y, et al. In-situ growing nickel phthalocyanine supramolecular structure on carbon nanotubes for efficient electrochemical CO_2 conversion[J]. Applied Catalysis B: Environmental, 2023, 327: 122446.

[51] Jiang Z, Zhang Z, Li H, et al. Molecular catalyst with near 100% selectivity for CO_2 reduction in acidic electrolytes[J]. Advanced Energy Materials, 2023, 13: 2203603.